Impact of multichance fission on fragment-neutron correlations in ^{227}Pa

N. Saneesh,[1,2,*] Divya Arora,[1] A. Chatterjee,[1] Neeraj Kumar,[3] Anamika Parihari,[4] Chandra Kumar,[1] I. Ahmed,[1] S. Kumar,[1] Mohit Kumar,[1] Akhil Jhingan,[1] K. S. Golda,[1] A. M. Vinodkumar,[2] and P. Sugathan[1]

[1]*Nuclear Physics division, Inter-University Accelerator Centre, Aruna Asaf Ali Marg, New Delhi - 110067, India*

[2]*Department of Physics, University of Calicut, Malappuram 673635, India*

[3]*GANIL, CEA/DRF - CNRS/IN2P3, Bd Henri Becquerel, BP 55027, F-14076 Caen Cedex 5, France*

[4]*Department of Physics and Astrophysics, University of Delhi, New Delhi-110007, India*

(Received 1 June 2023; accepted 11 August 2023; published 8 September 2023)

We investigate the influence of neutron emission in the fission of ^{227}Pa populated by complete fusion of ^{19}F with ^{208}Pb at various excitation energies (E^*). Mass gated pre-scission neutron multiplicities ($\nu_{\rm pre}$) were determined by fragment-neutron angular correlation and time of flight of fission fragments and neutrons using the National Array of Neutron Detectors facility. Obtained Mass $-$ $\nu_{\rm pre}$ correlation showed that, at lower $E^* = 24.2$ and 32.4 MeV, larger $\nu_{\rm pre}$ is correlated with asymmetric mass division. On the other hand, at higher $E^* = 46.1$ and 59.6 MeV, larger $\nu_{\rm pre}$ is correlated with symmetric mass division. The results were analyzed within the framework of the general description of fission observables GEneral description of Fission observables (GEF) model with multichance fission included. The analysis of fragment mass–total kinetic energy correlation for different chance fission clearly indicates a revival of shell effects at $E^* = 24.2$ and 32.4 MeV as a consequence of sequential fission decay. At these energies, higher chance fission decreases the saddle point excitation energy considerably where shell effects are prominent. The interplay of shell mediated mass asymmetric fission and symmetric fission gives rise to an energy dependent Mass $-$ $\nu_{\rm pre}$ correlation. We have compared the experimental results with Mass $-$ $\nu_{\rm pre}$ correlation predicted by the GEF model. It is concluded that the correlation of larger $\nu_{\rm pre}$ with asymmetric mass at lower excitation energies is a signature of shell effects reinstated by sequential fission decay. At the two higher excitation energies, despite the multichance fission and consequent decrease in saddle point energy, the available excitation energy appears sufficient for the attenuation of shell effects.

DOI: 10.1103/PhysRevC.108.034609

I. INTRODUCTION

From pioneering studies in the field of nuclear fission, it is well established that the shape evolution from a heavy nucleus to two fragment nuclei is determined by the interplay of macroscopic and microscopic nuclear properties [1–4]. In the actinide region, fission at higher excitation energies leads to symmetric distribution of fragment masses as predicted by the macroscopic liquid drop model [2]. On the other hand, mass distribution is generally found asymmetric at lower E^* [5]. The unequal division of the nucleus at lower E^* is interpreted as a manifestation of microscopic shell effects that modifies the potential energy surface (PES) of the fissioning nucleus [6,7]. Microscopic effects lead to distinct trajectories in the PES connecting the fissioning nucleus and the fragments with mass asymmetry [4]. This generally means that fission in the actinide region has bimodal (symmetric and asymmetric) characteristics. The coexistence of these symmetric and asymmetric modes are highly dependent on the E^* of the fissioning system [8]. Important features of bimodal fission observables are discussed in [9,10]. An overlap of these two distinct fission modes may occur when fission is preceded by particle emission, a phenomenon called multichance fission (MCF). Neutron emission reduces the initial E^* of the compound nucleus (CN) to $E^* - S_n - E_n$, where S_n is the neutron separation energy and E_n is the neutron kinetic energy. The valleys in the PES and the relative yields of symmetric and asymmetric fission fragments can be modified by this phenomenon. Chance fission occurs only at higher E^*, sufficient for allowing fission after neutron evaporation and it is important to account its probability for interpreting the observables of fission at higher excitation energies.

Recently, fission of actinide nuclei at higher E^* was investigated to understand the effect of neutron evaporation on fragment mass distribution [11–13]. In the experimental studies, fission in actinide targets was induced by a multinucleon transfer (MNT) process. The apparent mass-asymmetric fission at higher excitation energies ($\approx$60 MeV) was explained in light of MCF. Despite the high initial E^*, the multichance or sequential nature of fission decay restored the shell effects in these nuclei. Since pre-fission neutron emission is involved in reviving the shell effect, measurement of pre-scission neutron multiplicity ($\nu_{\rm pre}$) can also be used to study the nature of fission [14]. If neutrons are mainly emitted from the pre-saddle region, the average value of MCF can be obtained directly from $\nu_{\rm pre}$. Furthermore, the correlation between fragment mass and $\nu_{\rm pre}$ can also be used as a sensitive

*saneesh.iuac@gmail.com

probe for investigating the effect of MCF on mass distribution. Unlike fission induced by MNT, the full momentum transfer (FMT) process (e.g., in fusion reactions) results in the formation of neutron-deficient compound nuclei. The probability of higher chance fission is less in such systems compared to CN formed via MNT. Therefore, an early washout of the shell effects as a function of E^* can be expected in these nuclei [8]. However, if the MCF, particularly higher chance fission contributes significantly at any given excitation energy, the revival of microscopic effects needs to be invoked to explain the experimental results.

It is challenging to determine the probability or impact of a given fission chance since the experimental data are an admixture of all fission chances. However, theoretical calculations that consider MCF in the fission decay [13,15,16] can be used to determine the contribution of each chance to overall fission outcomes, if the calculation reproduces experimental observables. Average $\nu_{\rm pre}$ is one such observable that has a direct relationship with MCF probability. A comparison of experimental $\nu_{\rm pre}$ with theory for various E^* shall validate the MCF probability incorporated in the theoretical model. Validated MCF models can therefore be used to predict the influence of neutron emission on fission modes at different excitation energies. In parallel, the measurement of $\nu_{\rm pre}$ in correlation with fission fragment mass provides precise data on the role of pre-scission emission on mass division. Thus, a direct comparison between experiment with model prediction can be applied to deduce the influence of various fission chances on experimental observables. With this motivation, we measured the average $\nu_{\rm pre}$ and the Mass $-$ $\nu_{\rm pre}$ correlation for light actinide nuclei of ^{227}Pa formed in the complete fusion reaction of ^{19}F + ^{208}Pb in the E^* range ≈30–60 MeV. For a proper validation of the theory, average $\nu_{\rm pre}$ was measured at five E^* in this range. Mass $-$ $\nu_{\rm pre}$ correlation was investigated at low (32.4 MeV), medium (46.1 MeV) and high (59.6 MeV) excitation energies to figure out the role of MCF on fission modes. In an earlier investigation, the observed increase of fragment mass width at lower E^* was attributed to the interplay of asymmetric fission modes due to shells in the vicinity of ^{132}Sn [17]. A study of pre-scission neutrons and fragment mass-neutron correlation in this nucleus will confirm further the origin of asymmetric modes and the influence of neutron emission at higher excitation energies.

II. EXPERIMENTAL METHOD

Pulsed beams of ^{19}F projectiles, accelerated from the 15UD Pelletron accelerator at Inter University Accelerator Centre (IUAC), were used to bombard ^{208}Pb targets of thickness ≈250 μg/cm^2. Measurements were performed at laboratory energies of 90 MeV, 95 MeV, 100 MeV, 105 MeV, and 120 MeV. The target holder was mounted in the center of a 4 mm thick spherical vacuum chamber of 100 cm diameter. A schematic of the experimental setup is shown in Fig. 1. Fission fragments were detected in coincidence using two large area (20 cm × 10 cm) position sensitive multiwire proportional gas counters (MWPC1 and MWPC2) [18]. These counters were placed at 40° and 120°

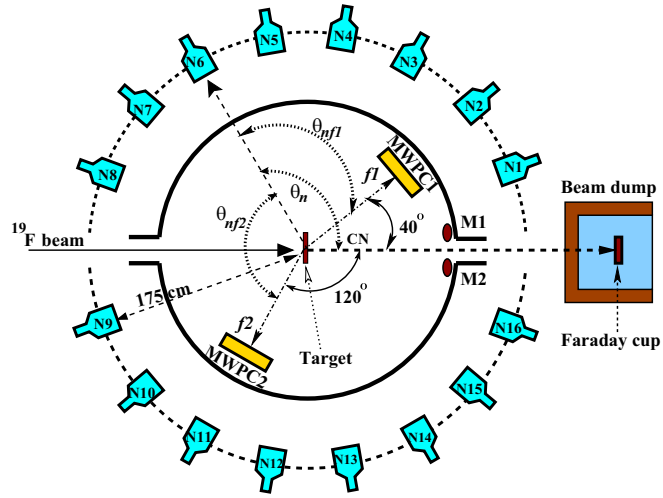

FIG. 1. Schematic view of the experiment setup used for measuring neutron multiplicity in coincidence with fission. θ_n, θ_{nf1}, and θ_{nf2} represent relative angles between various neutron sources [compound nucleus (CN), fragments $f1$ and $f2$] and neutron detectors. Neutron detectors (N1 to N16 of NAND array) in the reaction plane alone are displayed (see text for details).

angles on either side of the beam axis at a distance of 27 cm and 23 cm, respectively, from the target. The counters were operated with a continuous flow of isobutane gas maintained at a pressure of 4 mbar. The gas detector was isolated from the target chamber (pressure ≈4 × 10^{-6} mbar) using ≈0.9 μm mylar foil. Two planar silicon detectors (M1, M2) with a thickness of 300 μm were used to detect elastically scattered beam particles for continuous monitoring of the beam intensity.

Fast neutrons emitted in coincidence with the fission fragments were detected with the liquid scintillator array of the NAND facility [19]. Each detector consists of a 5 in. × 5 in. cell of BC501A liquid scintillator coupled to 5 in. diameter photomultiplier tube. These detectors were mounted at a distance of 175 cm from the target and positioned at selected coordinates of the geodesic dome structure of the NAND facility. To minimize background radiation, the beam was stopped in a beam dump placed 4.5 m downstream to the target and heavily shielded with thick layers of borated paraffin and lead. Bias voltages of all neutron detectors were optimized to achieve similar light output for known γ rays from radioactive sources (^{22}Na, ^{60}Co, ^{137}Cs). The neutron detection threshold was kept at ≈0.5 MeV for all detectors by adjusting the signal processing electronics. Zero crossover technique was used to discriminate between neutrons and γ rays using a pulse shape discrimination module [20]. The energy and angular distributions of fast neutrons were measured using the time of flight (TOF) method. The start signal to TOF measurement was generated by a coincidence between the radiofrequency (RF) of the beam pulse and the fission detector. VME based data acquisition was used to collect the list-mode data. Time of flight, pulse shape discrimination, and MWPC position signals were recorded online. Signal processing electronics

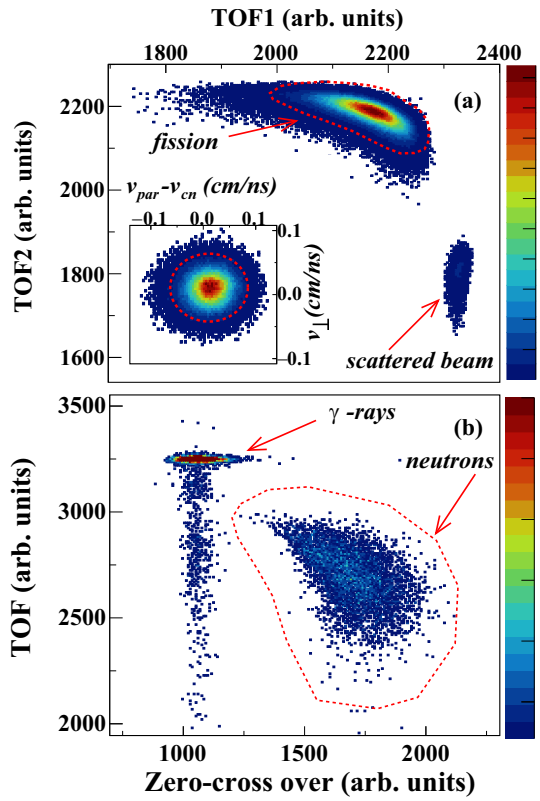

FIG. 2. (a) Time correlation of complementary events recorded in two MWPCs for the $^{19}F + ^{208}Pb$ reaction at 105 MeV. Events corresponding to fission fragments and scattered beam particles are indicated. The inset shows the velocity correlation plot for fission events derived from time of fight. (b) Plot of zero-cross time versus time of flight recorded in a neutron detector.

and neutron-gamma (n-γ) discrimination characteristics are detailed in Ref. [19].

III. DATA ANALYSIS AND RESULTS

The binary fission data was analyzed using the ROOT based analysis framework [22]. Fission fragments were separated from other charged particles such as scattered projectiles, target recoils, etc., by TOF and kinematic coincidence. Figure 2(a) shows the time correlation of events detected in MWPC1 and MWPC2. Fission events are selected for analysis of fragment mass and kinetic energy distributions by applying a graphical cut around the most intense region as shown in Fig. 2(a). The fission fragment mass and energy distributions were analyzed using the velocity reconstruction method described in Ref. [23]. From the x, y position coordinates and TOF, the velocity vectors of the two fragments and their projections on the parallel ($v_{\rm par}$) and perpendicular ($v_{\rm perp}$) planes with respect to the beam direction were extracted. The velocity components were corrected for energy loss in the target and entrance foil of MWPC. The two velocity components $v_{\rm par}$ and $v_{\rm perp}$ are used to separate the FMT fission events from the partial momentum transferred events [23]. The inset of Fig. 2(a) shows an example of the velocity correlation plot of fission events. A software cut around the centroid fixed at the value ($v_{\rm perp}$, $v_{\rm par} - v_{cn} = 0$, where v_{cn} is the compound-nucleus velocity) was applied to select FMT events. These selected events were further analyzed to determine the velocities of the fragments (V_1, V_2) in the center of mass frame (c.m.). The fission fragment mass ratio M_R and total kinetic energy (TKE) in the c.m. frame are expressed by

$$M_R = \frac{M_2}{(M_1 + M_2)} = \frac{V_1}{V_1 + V_2}, \tag{1}$$

$$\text{TKE} = \tfrac{1}{2}\left(M_1 \times V_1^2 + M_2 \times V_2^2\right). \tag{2}$$

The method used to extract pre-scission neutron multiplicity is based on fitting the neutron energy spectra at different angles using χ^2 minimization [24]. Excellent neutron-γ separation was obtained from TOF and zero-crossing time measurements. Figure 2(b) shows a two-dimensional (2D) histogram of the TOF versus zero-cross time from one of the neutron detectors. It can be seen that the neutron events are clearly separated from the γ-ray background. Applying a software cut around neutron events [shown by the dotted loop in Fig. 2(b)], the neutron TOF was converted to an energy histogram, considering the position of the prompt γ peak as the time reference. An energy-dependent efficiency correction was applied using the measured intrinsic efficiency of the neutron detector in the energy range of ≈0.5–10 MeV [25].

The kinematic effects on the energy and angular distributions of neutrons are assumed to originate from three moving sources (CN and two fission fragments), and the corresponding neutron spectra are described by the Watt distributions [24],

$$\frac{d^2M}{dE_n d\Omega_n} = \sum_{i=1}^{3} \frac{\nu_i \sqrt{E_n}}{2(\pi T_i)^{3/2}} \times \exp\left(-\frac{E_n + E_i/A_i - 2\cos\theta_i \sqrt{E_n E_i/A_i}}{T_i}\right), \tag{3}$$

where A_i, E_i, T_i, and ν_i are the mass number, kinetic energy, temperature, and multiplicity of each neutron emitting source i, respectively. E_n is the laboratory energy of the neutron and $d\Omega_n$ is the solid angle subtended by each BC501A detector. θ_i is the relative angle between neutron source and neutron detector. θ_n, θ_{nf1}, and θ_{nf2} shown in Fig. 1 represent the angles between the direction of neutron and neutron emitting sources such as CN, fragment 1 ($f1$), and fragment 2 ($f2$), respectively. Multiplicity ν_1 corresponds to the pre-scission neutron multiplicity $\nu_{\rm pre}$ and $\nu_{2,3}$ corresponds to neutrons emitted from a fission fragment, i.e., $\nu_{\rm post}$. The total neutron multiplicity is thus obtained as $M = \nu_{\rm pre} + 2 \times \nu_{\rm post}$. To extract $\nu_{\rm pre}$ and $\nu_{\rm post}$, a global fit to experimental spectra of $\mathrm{d}^2M/\mathrm{d}E_n\mathrm{d}\Omega_n$ was made in terms of the Watt expression, minimizing χ^2. To reduce any uncertainty in angles due to the large area of fission detectors, the data were analyzed only when the detected fragment was located within a rectangular slice of MWPC covering ±8°.

Figure 3 shows an example of the moving source fit to the experimental neutron multiplicity spectrum in the laboratory frame for $E^* = 46.1$ MeV. In Figs. 3(a) and 3(b), the double

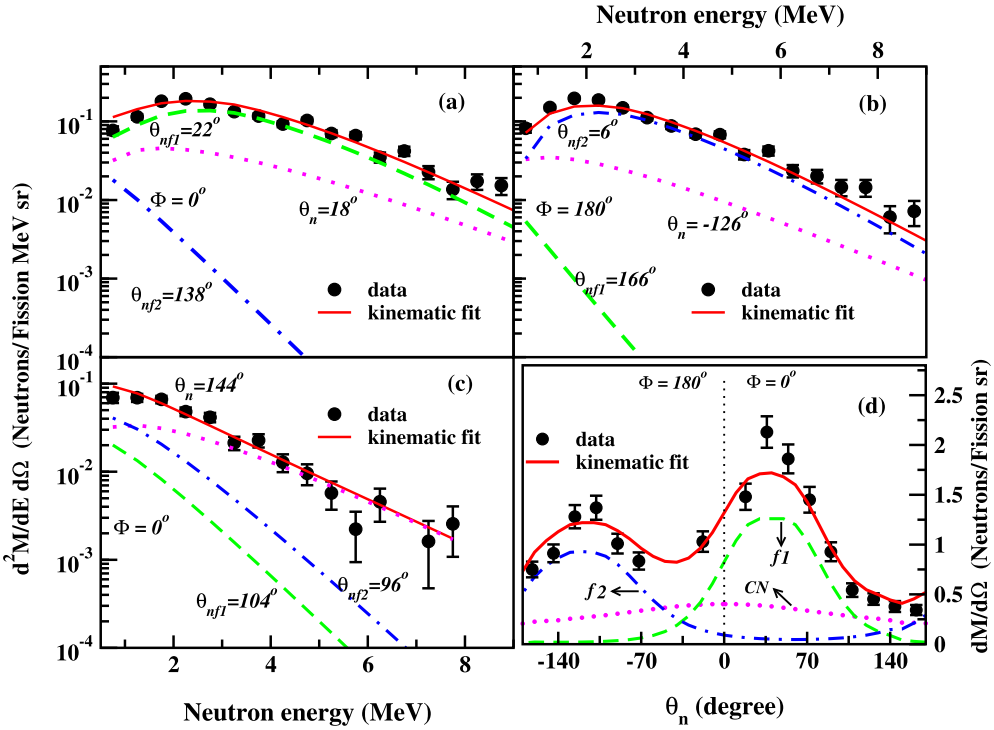

FIG. 3. (a)–(c) Examples of the three-moving-source fits to double differential neutron multiplicity spectra in the laboratory frame at various angles for the $^{19}F + ^{208}Pb$ reaction at 105 MeV beam energy. (d) Angular correlation of neutron yield $dM/d\Omega$ as a function of θ_n for detectors N1–N16. The contributions from individual neutron sources are indicated by curves; green dashed (fragment 1), blue dot-dashed (fragment 2), and pink dotted (CN source). The red solid line indicates total contributions from all sources and black solid circles denote data points with statistical errors. The dotted vertical line in (d) at $\theta_n = 0^\circ$ separates the data measured at $\Phi = 0^\circ$ and 180°.

differentials of neutron multiplicity are shown as a function of neutron energy for two NAND detectors near the MWPCs in the reaction plane. As expected, due to kinematic focusing, these spectra are dominated by contributions from their respective fission fragments. Figure 3(c) shows the fit result of the data from the NAND detector at backward angle. This spectrum shows the largest contribution from pre-scission neutrons (CN source). In Fig. 3(d), the derivative of the total neutron multiplicity $dM/d\Omega_n$ is plotted as a function of relative angle θ_n for 16 NAND detectors numbered N1 to N16 (see Fig. 1). It shows the contribution of three neutron emitting sources to the total neutron yield $dM/d\Omega_n$ at various angles and the corresponding value obtained from the kinematic fit. The excellent agreement between multiple moving-source fits and experimental spectra displayed in Figs. 3(a)–3(d) indicates the data are well described by three moving sources. The average ν_{pre} and ν_{post} extracted from the fitted spectra are listed in Table I.

To find the dependence of pre-scission neutron emission on the fragment mass, ν_{pre} was extracted for symmetric ($A = 108u$–$118u$) and asymmetric ($A = 128u$–$140u$) partition of mass distribution at $E^* = 32.4$ MeV ($\approx 4\%$ below the Coulomb barrier), 46.1 MeV and 59.6 MeV. The mass gated neutron multiplicities for measured energies are shown in Table I. The mass gated ν_{pre} for ^{227}Pa at $E^* = 24.2$ MeV reported in Ref. [21] is also included in Table I.

IV. DISCUSSION

To get further insight into the nature of fission and the correlation between various fission observables in CN ^{227}Pa and to compare with measurements, theoretical calculations were

TABLE I. Experimentally obtained pre-scission neutron multiplicities (average and mass-gated) of ^{227}Pa at different excitation energies.

E_{lab} (MeV)	E^* (MeV)	$\langle\nu_{pre}\rangle$	$\langle\nu_{post}\rangle$	$\langle\nu_{total}\rangle$	$\langle\nu_{pre}\rangle_{sym}$	$\langle\nu_{pre}\rangle_{asym}$
76.0	24.2	0.92 ± 0.14			0.81 ± 0.14	1.00 ± 0.14 [21]
90.0	32.4	1.44 ± 0.25	1.46 ± 0.08	4.36 ± 0.26	1.32 ± 0.31	1.60 ± 0.36
95.0	36.6	1.55 ± 0.22	1.64 ± 0.08	4.83 ± 0.23		
100.0	41.4	1.83 ± 0.18	1.53 ± 0.11	4.89 ± 0.21		
105.0	46.1	1.96 ± 0.25	1.85 ± 0.08	5.66 ± 0.26	2.01 ± 0.27	1.83 ± 0.33
120.0	59.6	2.58 ± 0.32	2.04 ± 0.11	6.66 ± 0.34	2.66 ± 0.35	2.43 ± 0.43

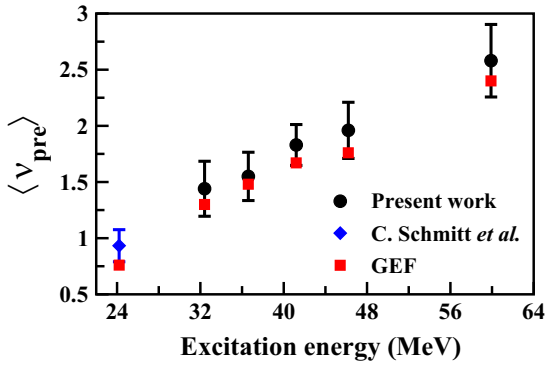

FIG. 4. Pre-scission neutron multiplicity measured for ^{227}Pa in the range of $E^* = 24.2$–59.6 MeV. Present measurements are shown as filled circles and previous measured data of Schmitt *et al*. [21] is denoted with a filled diamond. The GEF model prediction corresponding to each measurement is shown as filled squares.

performed using the GEneral description of Fission observables (GEF) model [15]. GEF is a semiempirical code widely used in low energy fission for describing fission observables and their correlations using global parameter values [26,27]. It describes the sequential decay of a nucleus specified by its excitation energy (E^*) and average angular momentum ($\langle l \rangle$). In the present study of ^{227}Pa formed in the fusion reaction $^{19}\mathrm{F} + ^{208}\mathrm{Pb}$ at various excitation energies, the $\langle l \rangle$ corresponding to each excitation energy was determined using the coupled-channels calculation code CCFULL [28]. The parameters of coupled-channels calculations were constrained by matching the measured fusion cross-section data [29,30] and the corresponding $\langle l \rangle$ values were obtained. GEF model calculations were performed for different values of (E^*, $\langle l \rangle$) corresponding to measured beam energies, taking into account the multichance fission in the CN decay scheme. The distributions of fission fragment mass, kinetic energy, neutron multiplicity, and their correlations were obtained from the list-mode output generated by GEF.

The pre-scission neutron multiplicity ν_{pre} is the sum of pre-saddle (ν_{ps}) and saddle to scission (ν_{ss}) neutron multiplicities. The pre-saddle neutron multiplicity can be related to various fission chances as

$$\langle \nu_{ps} \rangle = \frac{\sum_{i=1}^{n} (i-1) \times P_i^f}{\sum_{i=1}^{n} P_i^f}, \tag{4}$$

where P_i^f is the probability of fission for a given chance i. Post-saddle emission does not alter the observables or probability of fission [15,31]. In Fig. 4, the average ν_{pre} obtained from the GEF model calculation is compared with experiment results. The black filled circle symbols represent data from present measurement. The error bars shown are only statistical errors. The data represented using filled diamond symbol are from Ref. [21], where CN ^{227}Pa was studied using the reaction $^{18}\mathrm{O} + ^{209}\mathrm{Bi}$. The filled square symbols show the GEF results. It is observed that the GEF model reproduces the experimental data within error bars reasonably well across all measured energy in the range $E^* \approx 24$ MeV–60 MeV. This ascertains that sequential fission decay analysis incorporating specific yield to a given fission chance (P_i^f) can describe the experimental results. As particle emission lowers the excitation energy, the potential energy surface which governs the fission modes will be modified after each fission chance [4]. Therefore, analyzing the observables (mass distribution and kinetic energy) of each fission chance separately can give important information about the revival of shell effects on pre-saddle neutron emission. Since $\langle \nu_{\mathrm{pre}} \rangle$measurements validate the sequential fission decay scheme of GEF, the calculation has been extended to study the observables of each fission chance by analyzing GEF list-mode outputs at initial excitation energies $E^* = 59.6$ MeV, 46.1 MeV, 32.4 MeV, and 24.2 MeV where mass gated neutron multiplicity results have been obtained.

TABLE II. The GEF model calculation showing the probabilities of various fission chances, average saddle point energy, and pre-saddle multiplicity at different excitation energies of ^{227}Pa.

E^* (MeV)	fission chances	P_i^f (%)	$\langle E_{sp} \rangle_i$ (MeV)	$\langle \nu_{ps} \rangle$	$\langle E_{sp} \rangle$ (MeV)
59.6	1	7.4	59.6	2.24	38.1
	2	17.0	49.1		
	3	30.7	39.9		
	4	32.0	30.4		
	5	10.6	23.3		
46.1	1	11.6	46.1	1.76	30.0
	2	26.1	35.9		
	3	37.8	27.4		
	4	21.9	18.6		
32.4	1	17.6	32.4	1.30	20.8
	2	39.3	22.8		
	3	38.1	15.3		
	4	5.0	7.3		
24.2	1	34.7	24.2	0.76	17.5
	2	54.3	15.2		
	3	11.0	8.1		

A. Mass – TKE correlation

Measuring fission observables following each chance fission is a big experimental challenge. Generally, the experimental data will be an admixture of all chances averaged according to their probabilities. However, the contribution from each step of multichance fission can be theoretically investigated using the GEF code. For the present study of ^{227}Pa at four initial excitation energies, GEF predicted chance fission probabilities (P_i^f) are listed in Table II. Multichance fission with probability less than 5% is not considered here as it does not contribute significantly to the total fission yield. The average saddle point excitation energy ($\langle E_{sp} \rangle_i$) for a given chance fission i and the saddle point excitation energy averaged over all chances ($\langle E_{sp} \rangle$) are also given in Table II. The E_{sp} after particle emission is minimum for the last chance fission. Therefore the influence of fragment shells, if they exist, will be seen predominantly in the observables arising out of last chance fission. In low energy fission of actinide nuclei, shell effects give rise to asymmetric mass division with heavier mass centered around $A \approx 140$ and an

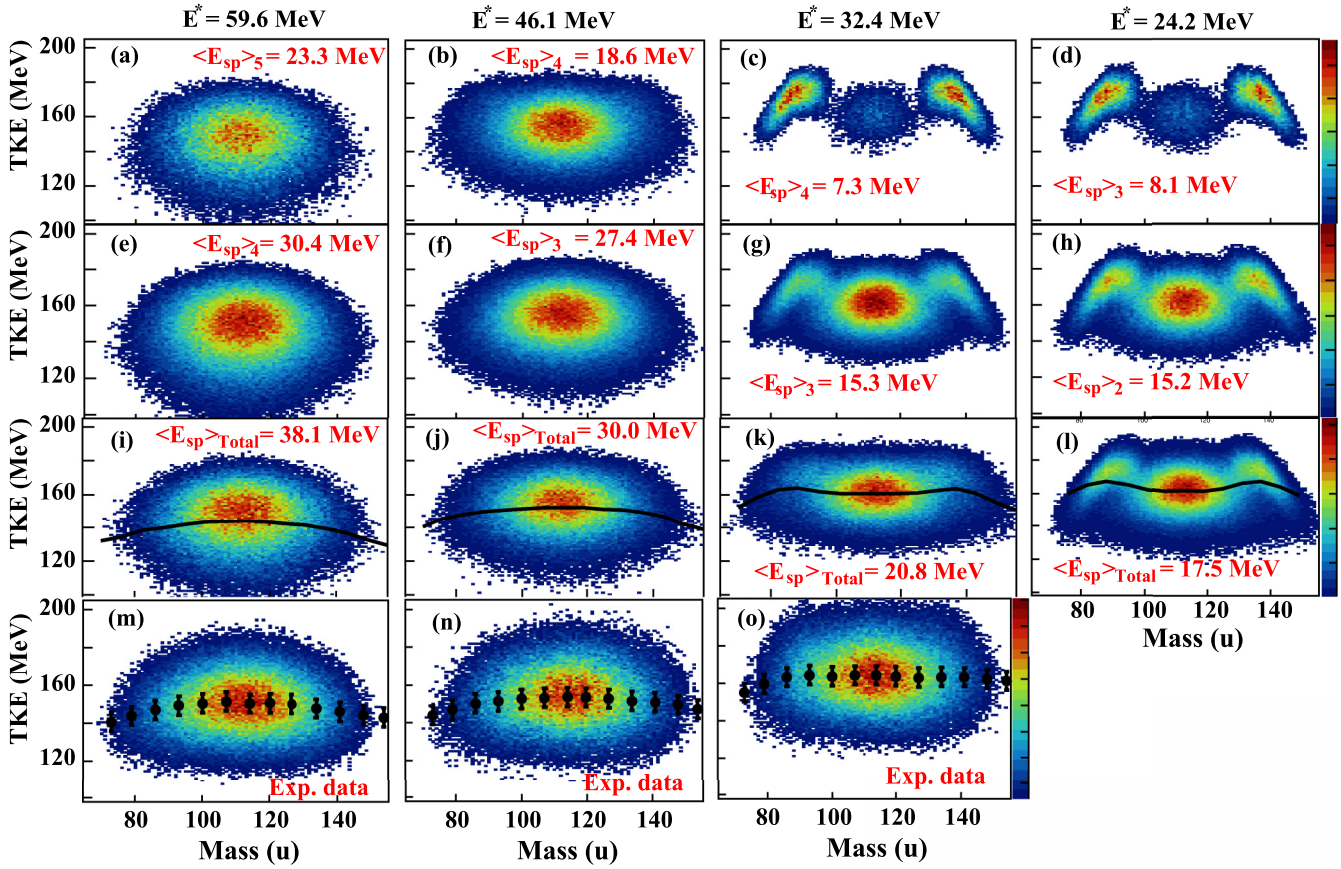

FIG. 5. Experimental and GEF predicted Mass − TKE correlations for ^{227}Pa at $E^* = 59.6$, 46.1, 32.4, and 24.2 MeV. The upper panels (a)–(d) and (e)–(h) correspond to GEF produced Mass − TKE spectra corresponding to last and second-to-last chance fissions, respectively. (i)–(l) represent GEF produced Mass − TKE correlations with the contribution of all chance fission summed according to their probabilities. The solid lines represent the mean TKE as a function of fragment mass. Measured Mass − TKE correlations are shown in (m)–(o). The filled circles (black) represent the average TKE for given mass bin. See the text for details.

increase in TKE due to the compact configuration of nascent fragments [10].

From GEF list-mode output, the Mass-TKE correlations were determined separately for each chance fission. The results for the final two chances of fission and the overall average contribution are illustrated in Fig. 5 [panels (a) through (l)] for $E^* = 59.6$ MeV, 46.1 MeV, 32.4 MeV, and 24.2 MeV, respectively. The Mass − TKE correlation from events of last chance fission alone are shown in the upper panels (a), (b), (c), and (d). Corresponding $\langle E_{sp}\rangle_i$ are noted in the panels. The Mass − TKE plot of the last chance fission [panels (c) and (d)] clearly identifies shell induced mass asymmetric fission for $E^* = 32.4$ MeV and 24.2 MeV. While even the last chance fission does not reveal any detectable signs of shells for initial $E^* = 59.6$ MeV. Similar findings may be seen in the Mass − TKE correlation plots shown in panels (e) through (h) of Fig. 5. These plots show second-to-last chance fission distributions, and the associated $\langle E_{sp}\rangle_i$ are higher compared to last chance fission distributions. As anticipated, these correlation plots [Figs. 5(g) and 5(h)] too show the influence of shell effects but less than those of last chance fission events. Figure 5, panels (i), (j), (k), and (l) display the overall Mass − TKE distribution taking into account all chance fission. Panels (m), (n), and (o) represent measured Mass − TKE distributions corresponding to $E^* = 59.6$, 46.1, and 32.4 MeV, respectively. GEF data were purposefully broadened by the current experimental mass resolution of $\sigma_m = 5u$ in order to take finite mass resolution effects into consideration. The solid line represents the GEF predicted average TKE as a function of fragment mass. The solid circle represents the averaged TKE over the $5u$ mass bin. The GEF predicted Mass − TKE distribution taking into account all chances closely matched with measured data at three measured energies. The average TKE exhibits a parabolic dependence on fragment mass in both measurement and GEF results at $E^* = 59.6$ MeV and 46.1 MeV. The average TKE is found to be virtually constant over a range of fragment masses and somewhat higher for asymmetric masses at $E^* = 32.4$ MeV, as shown in Figs. 5(k) and 5(o). However, noticeable asymmetric mass shoulders are not visible in the measured spectrum. At this energy, shell effects cause a significant amount of asymmetric fission component and an increase in kinetic energy in the third and fourth chance fission, which modifies the overall Mass − TKE distribution. Therefore, asymmetric fission modes at higher chance fission may be attributed for the change in Mass − TKE distribution observed when the excitation energy was reduced from

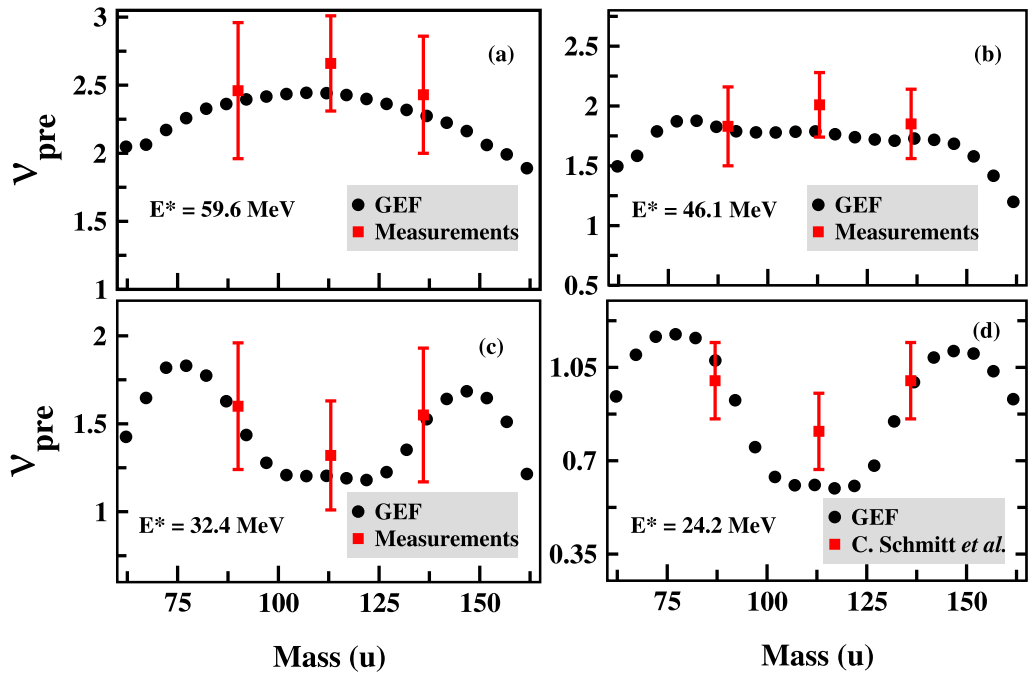

FIG. 6. Correlation between experimental ν_{pre} and fragment mass compared with the GEF model calculation for ^{227}Pa at $E^* = 59.6$, 46.1, 32.4, and 24.2 MeV. Filled squares with error bars denote the ν_{pre} extracted from symmetric and asymmetric mass cuts to total mass distribution. Data of $E^* = 24.2$ MeV are from Schmitt *et al*. [21].

59.6 MeV to 32.4 MeV [Figs. 5(g) and 5(i)]. A closer look at Mass − TKE distributions in panels (b), (f), (j), and (n) of Fig. 5 suggest the transition from symmetric fission to asymmetric fission may occur at $E^* \approx 46$ MeV.

B. Mass − ν_{pre} correlation

To determine the dependence of ν_{pre} on fragment mass, we further analyzed the GEF output for mass distribution corresponding to each chance fission for a given excitation energy. The mass gated pre-scission neutron multiplicity, ν^M_{pre} was calculated using the expression

$$\nu^M_{\text{pre}} = \frac{\sum_{i=1}^{n}(i-1)\times N_i^M}{\sum_{i=1}^{n} N_i^M}, \tag{5}$$

where N_i^M is the fission yield for a given fragment mass M. The value of N_i^M for a given mass bin was obtained by averaging the multichances according to their probability. The variation of ν_{pre} as a function of fragment mass is summarized in Fig. 6. GEF results are compared to present measurements made at 59.6 MeV [Fig. 6(a)], 46.1 MeV [Fig. 6(b)], and 32.4 MeV [Fig. 6(c)]. Figure 6(d) shows a comparison of mass gated pre-scission neutron multiplicity of ^{227}Pa at 24.2 MeV reported in [21] with GEF calculation. According to GEF, due to multichance fission, shell effects are prevalent at this excitation energy which is displayed in Figs. 5(d), 5(h), and 5(l).

At $E^* = 59.6$ MeV and 46.1 MeV, the measured data show higher ν_{pre} for symmetric mass division than for asymmetric mass. Similar findings were reported for compound nuclei at high excitation energies [32,33]. This is attributed to the difference in the timescales of symmetric and asymmetric fission of the system at higher excitation energies [32]. At lower excitation energies, 32.4 MeV and 24.2 MeV [Figs. 6(c) and 6(d)], higher ν_{pre} correlates with asymmetric fission. GEF calculations that account for the multichance nature of fission reproduce similar Mass − ν_{pre} correlations at these energies. This indicates that at these two energies, multichance fission strongly influences the fission mode. Mass − TKE correlation shown in Fig. 5 also unambiguously indicates the presence of shell effects at higher fission chances for $E^* = 32.4$ MeV and 24.2 MeV. The chance fission probabilities given in Table II for 32.4 MeV shows that ≈43% of fission occurs at $\langle E_{sp}\rangle \approx$ 14.4 MeV (chance 3 and 4 where the presence of shell effect was observed). Similarly, at $E^* = 24.2$ MeV, the second and third chance (where shell effects were noticed) fission together account for ≈65% of fission at $\langle E_{sp}\langle \approx 13.9$ MeV. This suggests that even though the compound nucleus was formed at E^* of 32.4 MeV and 24.2 MeV, pre-saddle neutron emission leads to the restoration of the shell effects when the excitation energy at the saddle point is greatly reduced, leading to asymmetric fission.

In the event of higher pre-saddle neutron emission and resultant decrease in excitation energy, microscopic shell effect modify the potential energy surface of the fissioning nucleus. Shell effect enhances the probability of asymmetric fission path on the PES as the saddle point excitation energy decreases. Higher pre-saddle neutron emission and consequent mass asymmetric fission give rise to the observed Mass − ν_{pre} correlations as displayed in Figs. 6(c) and 6(d). It can be observed from Figs. 6(c) and 6(d) that the nucleus tends to go to asymmetric fission when more neutrons are emitted. Asymmetric fission is enhanced by pre-saddle neutron emission and a consequent decrease in saddle point energy, which would

be less significant if the compound nucleus undergoes fission at its initial excitation energy. Therefore, the correlation of larger $\nu_{\rm pre}$ with asymmetric mass division can be interpreted as a feature of the fragment shell effect reinstated by multichance fission of actinide nucleus ^{227}Pa. For $E^* = 59.6$ MeV and 46.1 MeV, GEF calculations predict multichance fission and an overall decrease in E_{sp} as shown in Table II. However, neither Mass − TKE nor Mass − $\nu_{\rm pre}$ distributions show significant evidence of shell-mediated asymmetric fission. In other words, the saddle point excitation energy was sufficient for the attenuation of shell effects in ^{227}Pa formed at energies of 59.6 MeV and 46.1 MeV. In contrast, fission of neutron-rich compound nuclei formed by the MNT process shows evidence of shells even at higher E^* up to ≈60 MeV [11,12]. The dynamical model calculation using the Langevin approach by including MCF successfully reproduced these experimental mass spectra [13]. In neutron-rich CN, the neutron emission probability is higher than fission [13,15,34] and $\langle E_{sp}\rangle$ of the fissioning nucleus is reduced, promoting shell-mediated mass asymmetric fission. The present work, together with works by others [11–13,16], shows that the fission observables in these two extreme scenarios (neutron-deficient CN formed by FMT and neutron-rich CN formed by MNT) can be explained by the proper inclusion of pre-saddle particle emission and the resulting saddle point excitation energy.

V. SUMMARY AND CONCLUSION

Using fragment-neutron angular correlation, we have determined the prompt neutron multiplicities in the fission of ^{227}Pa populated by ^{19}F + ^{208}Pb complete fusion at different excitation energies. The measurements were carried out for excitation energies as low as 32.4 MeV, which is ≈4% below the Coulomb barrier and up to $E^* = 59.6$ MeV. The influence of pre-scission neutron emission on mass division (symmetric or asymmetric) of ^{227}Pa was determined by investigating the variation of pre-scission neutron multiplicity as a function of fragment mass. Semiempirical calculations within the framework of the GEF model incorporating the multichance nature of fission were carried out to determine the Mass − TKE and Mass − $\nu_{\rm pre}$ correlations in ^{227}Pa at measured excitation energies. The sequential fission decay incorporated in the GEF model was ascertained by comparing the $\langle\nu_{\rm pre}\rangle$ at multiple energies with measurement.

For each excitation energy, the Mass − TKE distribution corresponding to different fission chances was examined using the GEF model. From this, it is concluded that there is no noticeable asymmetric fission mediated by shell effects at $E^* = 59.6$ MeV and 46.1 MeV according to Mass − TKE correlation. Whereas, at $E^* = 32.4$ and 24.2 MeV, the average TKE is found to be virtually constant over a range of fission fragment masses. This change in Mass − TKE distribution as compared to the corresponding spectra at $E^* = 59.6$ MeV and 46.1 MeV is attributed to the existence of asymmetric fission modes due to higher chance fission. The experimental Mass − TKE distributions at these energies agree well with the overall trend anticipated by the GEF calculation.

In light of multichance fission, we have demonstrated the theoretical distribution of pre-scission neutron multiplicity as a function of fragment mass. The measured Mass − $\nu_{\rm pre}$ correlation and its variation with excitation energy are in good agreement with predictions from the GEF model. At higher excitation energies (46.1 MeV and 59.6 MeV), $\nu_{\rm pre}$ was seen to be larger for symmetric fission as reported in literature. However, higher $\nu_{\rm pre}$ was correlated with asymmetric mass division at lower excitation energies (24.2 MeV and 32.4 MeV). According to GEF calculations, higher chance fission significantly reduces the saddle point energy (E_{sp}) at these excitation energies. For instance, at $E^* = 32.4$ MeV, ≈43% of the fission occurs at $\langle E_{sp}\rangle \approx 14.4$ MeV due to pre-saddle neutron emission. Similarly, at 24.2 MeV, $\langle E_{sp}\rangle$ is ≈13.9 MeV for 65% of fission. At these lower saddle point energies, shell effects are prominent which give rise to an interplay of asymmetric fission modes. From these results, it is concluded that the correlation of higher $\nu_{\rm pre}$ with asymmetric fission than symmetric fission is a signature of shell effects reinstated by sequential fission decay. Though the ^{227}Pa nucleus populated at 46.1 and 59.6 MeV also exhibit multichance fission and resultant decrease in saddle point excitation energy, the available excitation energy appears sufficient for the attenuation of shell effects.

ACKNOWLEDGMENTS

Authors gratefully acknowledge the fruitful discussions with Prof. K.-H. Schmidt during the preparation of the manuscript. Authors acknowledge the IUAC Pelletron accelerator group for providing a good quality pulsed beam and the Target laboratory for providing thin ^{208}Pb targets.

[1] L. Meitner and O. R. Frisch, Nature (London) **143**, 239 (1939).
[2] N. Bohr and J. A. Wheeler, Phys. Rev. **56**, 426 (1939).
[3] V. S. Ramamurthy, S. S. Kapoor, and S. K. Kataria, Phys. Rev. Lett. **25**, 386 (1970).
[4] P. Möller, D. G. Madland, A. J. Sierk, and A. Iwamoto, Nature (London) **409**, 785 (2001).
[5] A. Turkevich and J. B. Niday, Phys. Rev. **84**, 52 (1951).
[6] V. Strutinsky, Nucl. Phys. A **95**, 420 (1967).
[7] V. Strutinsky, Nucl. Phys. A **122**, 1 (1968).
[8] A. V. Ignatyuk, G. N. Smirenkin, and A. S. Tishin, Sov. J. Nucl. Phys. **21**, 255 (1975) [Yad. Fiz. **21**, 485 (1975)].
[9] E. K. Hulet, J. F. Wild, R. J. Dougan, R. W. Lougheed, J. H. Landrum, A. D. Dougan, M. Schadel, R. L. Hahn, P. A. Baisden, C. M. Henderson, R. J. Dupzyk, K. Sümmerer, and G. R. Bethune, Phys. Rev. Lett. **56**, 313 (1986).
[10] U. Brosa, S. Grossmann, and A. Müller, Phys. Rep. **197**, 167 (1990).
[11] R. Léguillon, K. Nishio, K. Hirose, H. Makii, I. Nishinaka, R. Orlandi, K. Tsukada, J. Smallcombe, S. Chiba, Y. Aritomo, T. Ohtsuki, R. Tatsuzawa, N. Takaki, N. Tamura, S. Goto, I. Tsekhanovich, C. Petrache, and A. Andreyev, Phys. Lett. B **761**, 125 (2016).

[12] K. Hirose, K. Nishio, S. Tanaka, R. Léguillon, H. Makii, I. Nishinaka, R. Orlandi, K. Tsukada, J. Smallcombe, M. J. Vermeulen, S. Chiba, Y. Aritomo, T. Ohtsuki, K. Nakano, S. Araki, Y. Watanabe, R. Tatsuzawa, N. Takaki, N. Tamura, S. Goto, I. Tsekhanovich, and A. N. Andreyev, Phys. Rev. Lett. **119**, 222501 (2017).
[13] S. Tanaka, Y. Aritomo, Y. Miyamoto, K. Hirose, and K. Nishio, Phys. Rev. C **100**, 064605 (2019).
[14] M. Itkis, L. Calabretta, F. Hanappe, Y. Itkis, A. Kelic, N. Kondratiev, E. Kozulin, Y. Oganessian, I. Pokrovsky, E. Prokhorova, G. Rudolf, A. Rusanov, and L. Stuttge, Nucl. Phys. A **654**, 870c (1999).
[15] K.-H. Schmidt, B. Jurado, C. Amouroux, and C. Schmitt, Nucl. Data Sheets **131**, 107 (2016).
[16] A. C. Berriman, D. J. Hinde, D. Y. Jeung, M. Dasgupta, H. Haba, T. Tanaka, K. Banerjee, T. Banerjee, L. T. Bezzina, J. Buete, K. J. Cook, S. Parker-Steele, C. Sengupta, C. Simenel, E. C. Simpson, M. A. Stoyer, B. M. A. Swinton-Bland, and E. Williams, Phys. Rev. C **105**, 064614 (2022).
[17] R. Dubey, P. Sugathan, A. Jhingan, G. Kaur, I. Mukul, G. Mohanto, D. Siwal, N. Saneesh, T. Banerjee, M. Thakur, R. Mahajan, N. Kumar, and M. Chatterjee, Phys. Lett. B **752**, 338 (2016).
[18] A. Jhingan, N. Saneesh, M. Kumar, R. Mahajan, M. Thakur, G. Kaur, K. Kapoor, N. Kumar, M. Shareef, R. Dubey, S. Appannababu, E. Prasad, H. Singh, K. S. Golda, R. Ahuja, B. R. Behera, and P. Sugathan, Rev. Sci. Instrum. **92**, 033309 (2021).
[19] N. Saneesh, K. Golda, A. Jhingan, S. Venkataramanan, T. Varughese, M. Kumar, M. Thakur, R. Mahajan, B. Behera, P. Sugathan, A. Chatterjee, and M. Chatterjee, Nucl. Instrum. Methods Phys. Res. A **986**, 164754 (2021).
[20] S. Venkataramanan, A. Gupta, K. S. Golda, H. Singh, R. Kumar, R. P. Singh, and R. K. Bhowmik, Nucl. Instrum. Methods Phys. Res. A **596**, 248 (2008).
[21] C. Schmitt, J. Bartel, A. Surowiec, and K. Pomorski, Acta Phys. Pol. B **34**, 2135 (2003).
[22] R. Brun and F. Rademakers, Nucl. Instrum. Methods Phys. Res. A **389**, 81 (1997).
[23] D. J. Hinde, M. Dasgupta, J. R. Leigh, J. C. Mein, C. R. Morton, J. O. Newton, and H. Timmers, Phys. Rev. C **53**, 1290 (1996).
[24] B. E. Watt, Phys. Rev. **87**, 1037 (1952).
[25] N. Saneesh, D. Arora, A. Chatterjee, K. Golda, M. Kumar, A. Vinodkumar, and P. Sugathan, Nucl. Instrum. Methods Phys. Res. A **1013**, 165682 (2021).
[26] K.-H. Schmidt and B. Jurado, Rep. Prog. Phys. **81**, 106301 (2018).
[27] C. Schmitt, K.-H. Schmidt, and B. Jurado, Phys. Rev. C **98**, 044605 (2018).
[28] K. Hagino, N. Rowley, and A. Kruppa, Comput. Phys. Commun. **123**, 143 (1999).
[29] Z. Huanqiao, L. Zuhua, X. Jincheng, X. Kan, L. Jun, and R. Ming, Nucl. Phys. A **512**, 531 (1990).
[30] D. J. Hinde, A. C. Berriman, M. Dasgupta, J. R. Leigh, J. C. Mein, C. R. Morton, and J. O. Newton, Phys. Rev. C **60**, 054602 (1999).
[31] A. V. Karpov, P. N. Nadtochy, D. V. Vanin, and G. D. Adeev, Phys. Rev. C **63**, 054610 (2001).
[32] D. J. Hinde, D. Hilscher, H. Rossner, B. Gebauer, M. Lehmann, and M. Wilpert, Phys. Rev. C **45**, 1229 (1992).
[33] D. Hilscher and H. Rossner, Ann. Phys. (Paris) **17**, 471 (1992).
[34] M. Sin, R. Capote, M. Herman, and A. Trkov, Nucl. Data Sheets **139**, 138 (2017).